Earth, Planets and Space

FULL PAPER Open Access

Electromagnetic conjugacy of ionospheric disturbances after the 2022 Hunga Tonga-Hunga Ha'apai volcanic eruption as seen in GNSS-TEC and SuperDARN Hokkaido pair of radars observations

Atsuki Shinbori[1*], Yuichi Otsuka[1], Takuya Sori[1], Michi Nishioka[2], Septi Perwitasari[2], Takuo Tsuda[3] and Nozomu Nishitani[1]

Abstract

To elucidate the characteristics of electromagnetic conjugacy of traveling ionospheric disturbances just after the 15 January 2022 Hunga Tonga-Hunga Ha'apai volcanic eruption, we analyze Global Navigation Satellite System-total electron content data and ionospheric plasma velocity data obtained from the Super Dual Auroral Radar Network Hokkaido pair of radars. Further, we use thermal infrared grid data with high spatial resolution observed by the Himawari 8 satellite to identify lower atmospheric disturbances associated with surface air pressure waves propagating as a Lamb mode. After 07:30 UT on 15 January, two distinct traveling ionospheric disturbances propagating in the westward direction appeared in the Japanese sector with the same structure as those at magnetically conjugate points in the Southern Hemisphere. Corresponding to these traveling ionospheric disturbances with their large amplitude of $0.5 - 1.1 \times 10^{16}$ el/m^2 observed in the Southern Hemisphere, the plasma flow direction in the F region changed from southward to northward. At this time, the magnetically conjugate points in the Southern Hemisphere were located in the sunlit region at a height of 105 km. The amplitude and period of the plasma flow variation are ~ 100–110 m/s and ~ 36–38 min, respectively. From the plasma flow perturbation, a zonal electric field is estimated as ~ 2.8–3.1 mV/m. Further, there is a phase difference of ~ 10–12 min between the total electron content and plasma flow perturbations. This result suggests that the external electric field variation generates the traveling ionospheric disturbances observed in both Southern and Northern Hemispheres. The origin of the external electric field is an E-region dynamo driven by the neutral wind oscillation associated with atmospheric acoustic waves and gravity waves. Finally, the electric field propagates to the F region and magnetically conjugate ionosphere along magnetic field lines with the local Alfven speed, which is much faster than that of Lamb mode waves. From these observational facts, it can be concluded that the E-region dynamo electric field produced in the sunlit Southern Hemisphere is a main cause of the two distinct traveling ionospheric disturbances appearing over Japan before the arrival of the air pressure disturbances.

Keywords: Electromagnetic conjugacy of traveling ionospheric disturbances, 2022 Hunga Tonga-Hunga Ha'apai volcanic eruption, GNSS-TEC and SuperDARN Hokkaido radar observations

*Correspondence: shinbori@isee.nagoya-u.ac.jp

[1] Institute for Space-Earth Environmental Research (ISEE), Nagoya University, Nagoya, Aichi 464-8601, Japan
Full list of author information is available at the end of the article

Graphical Abstract

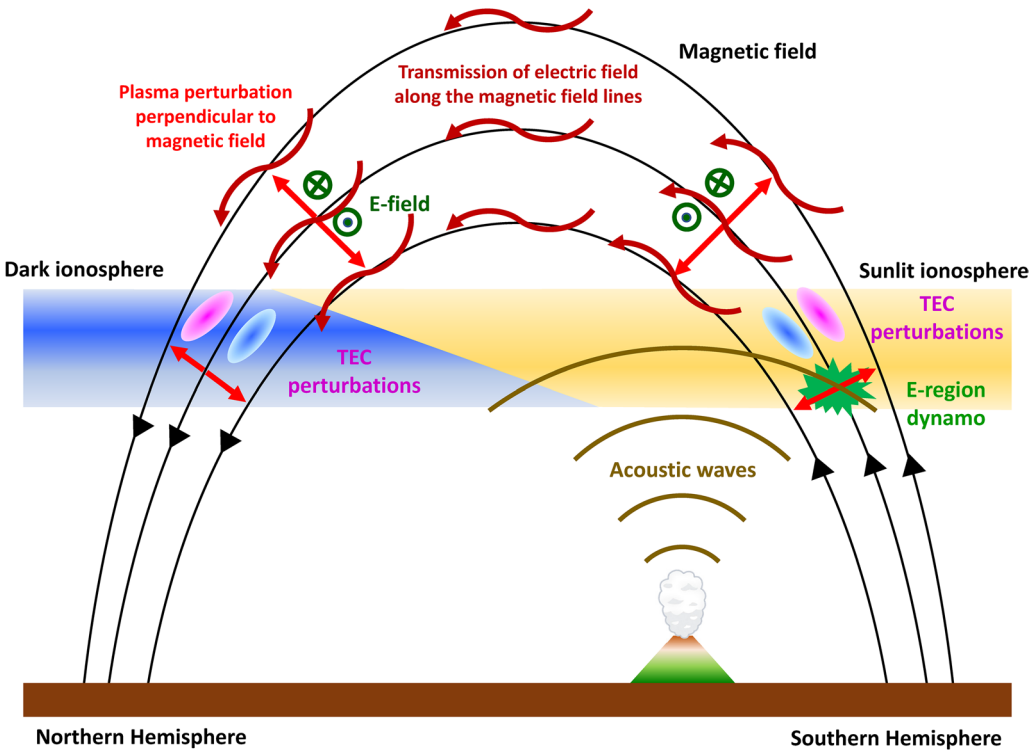

Main text

Introduction

The Earth's ionosphere is formed by ionization of upper atmosphere due to solar EUV radiation and energetic particle precipitation from the sun and magnetosphere. The spatial distribution of plasma density in the ionosphere shows a strong dependence on latitude, longitude, local time, season, and solar activity (e.g., Kelley 2009). Because the ionosphere consists of partially ionized layers where the charged particles frequently collide with the neutral atmosphere, perturbations in the neutral atmosphere cause a change in plasma density distribution in the ionosphere and a dynamo electric field through momentum transfer by ion-neutral collisions (e.g., Maeda and Kato 1966; Richmond 1979). The dynamo electric field drives $\mathbf{E} \times \mathbf{B}$ drift of ionospheric plasma and propagates along magnetic field lines with a local Alfven speed in the F region of the ionosphere and the plasmasphere (e.g., Yamazaki and Maute 2017). The $\mathbf{E} \times \mathbf{B}$ drift leads to the spatial inhomogeneity or gradient of plasma density and conductivity in the ionosphere. The gradient of the ionospheric conductivity creates polarization electric field to keep the current continuity. The neutral atmospheric perturbations, dynamo, and polarization electric fields generate TIDs observed as ionospheric TEC variations.

Volcanic eruptions, earthquakes, tsunami, and atmospheric convective systems cause atmospheric acoustic waves, AGWs and RWs in the lower atmosphere and ocean (Mayr et al. 1984a, b; Ajith et al. 2020), which generate the TIDs in the ionosphere (e.g., Choosakul et al. 2009; Heki 2006; Liu et al. 2011; Otsuka et al. 2006; Rolland et al. 2011; Saito et al. 2011; Tsugawa et al. 2011; Nishioka et al. 2013; Chou et al. 2017; Astafyeva 2019; Inchin et al. 2020). The 2011 Tohoku earthquake and tsunami generated concentric LSTIDs with a propagation speed of ~3.5 km/s in association with an RW (e.g., Galvan et al. 2012; Jin et al. 2015; Kakinami et al. 2013; Liu et al. 2011; Rolland et al. 2011). After the LSTID phenomena, MSTIDs with their propagation speed of 138–423 m/s were observed (Tsugawa et al. 2011). Savastano et al. (2017) found that TIDs with their propagation speed of 316 m/s are triggered by the 2012 Haida Gwaii earthquake and that the propagation speed agrees well with that of acoustic waves in the atmosphere. Shults et al. (2016) showed that acoustic waves propagating in the ionosphere with a phase speed of 900–1200 m/s were generated by the eruption of the Calbuco volcano on

22–23 April 2015. They also pointed out that the phase speed is similar to that of the acoustic waves triggered by three other volcano events shown in previous studies (Heki 2006; Dautermann et al. 2009a, 2009b; Nakashima et al. 2016). Nakashima et al. (2016) found that the TEC variations with three frequency ranges of 3.7, 4.8, and 6.8 mHz were observed after the 2014 eruption of the Kelud volcano. However, because the observed region of ionospheric disturbances triggered by the acoustic waves reported in the above events was limited within about 1000 km of the volcano source, electromagnetic conjugacy and global propagation nature of TIDs generated by volcanic eruptions have not yet been clarified.

The recent Hunga Tonga-Hunga Ha'apai volcanic eruption with VEI of 6 (Poli and Shapiro 2022) occurred at 04:10 UT on 15 January 2022 and a height of the volcanic plume reached 50–55 km near the stratopause or lower mesosphere (Carr et al. 2022). The large eruption generated the shock waves rippling through the air that vibrate the entire atmosphere. The images of NASA Earth observation satellites showed Lamb waves circulating the Earth, and the Lamb waves were observed as multiple air pressure waves by worldwide ground weather stations (Duncombe 2022; Imanishi 2022). The air pressure waves caused tsunamis through the air–sea coupling process (Carvajal et al., 2022; Tanioka et al. 2022). The atmospheric disturbances related to the violent eruption triggered atmospheric acoustic waves and AGWs (Adam 2022) that generate plasma density perturbations in the ionosphere (Astafyeva et al. 2022; Lin et al. 2022; Saito 2022; Themens et al. 2022). Actually, various types of TID signatures globally appeared in two-dimensional maps of detrended TEC obtained from many GNSS stations for several days after the Hunga Tonga-Hunga Ha'apai volcanic eruption. Further, the MSTIDs propagating westward over Japan were observed several hours before the arrival of the Lamb wave front. In this study, we clarify the characteristics and generation mechanism of the MSTIDs propagating westward over Japan using GNSS-TEC and SuperDARN Hokkaido pair of radars observation data with high time and spatial resolutions.

Observation data and analysis method

Observation datasets

To investigate the temporal and spatial variations of TEC associated with the 2022 Hunga Tonga-Hunga Ha'apai volcanic eruption, we use GNSS-TEC data with time resolution of 30 s derived from GNSS data. These GNSS data are obtained from many GNSS receivers all over the world. The number of GNSS stations are more than 8000 in January 2022. These data were provided by 50 data providers listed on the GNSS-TEC website at Nagoya University (http://stdb2.isee.nagoya-u.ac.jp/GPS/GPS-TEC/gnss_provider_list.html). To find electric field perturbations that create the TEC variations triggered by the Tonga volcanic eruption, we use line-of-site plasma velocity data in the ionosphere observed by the SuperDARN Hokkaido pair of radars. An overview of the SuperDARN radars has been described by Nishitani et al. (2019). Time resolution of the line-of-site plasma velocity data is 1 min. To identify spatial and temporal evolutions of lower atmospheric disturbances associated with the Tonga volcanic eruption, we use TIR grid data of 6.2 μm wavelength with spatial resolution of $0.02^{o} \times 0.02^{o}$ in geographical latitude and longitude obtained from the Himawari 8 satellite (Takenaka et al. 2020; Yamamoto et al. 2020). Time resolution of the TIR data is 10 min. The Himawari 8 satellite TIR grid data were provided by the CEReS, Chiba University (http://www.cr.chiba-u.jp/databases/GEO/H8_9/FD/index_en_V20190123.html). Further, we use high resolution OMNI (HRO) data of the Bz component of the IMF in GSM coordinates, solar wind proton density and speed with time resolution of 1 min provided by the NASA CDAWeb (https://cdaweb.sci.gsfc.nasa.gov/index.html/), the AE index (World Data Center for Geomagnetism et al. 2015) and the SYM-H index (Iyemori 1990; Iyemori and Rao 1996; World Data Center for Geomagnetism et al. 2022) provided by the World Data Center for Geomagnetism, Kyoto University (http://wdc.kugi.kyoto-u.ac.jp/index.html). These OMNI and geomagnetic indices are used to investigate solar wind and geomagnetic conditions during a period when the TIDs and plasma flow perturbations are triggered by the Tonga volcanic eruption. To obtain magnetically conjugate points in between the Northern and Southern Hemispheres, we use the IGRF-13 model (Alken et al. 2021).

Analysis method

In this study, we analyze 15-min detrended vertical TEC values with spatial resolution of $0.25^{o} \times 0.25^{o}$ in geographic latitude and longitude. The detrended TEC values are derived from subtracting the 15-min running average of relative TEC values. They are obtained from a difference of the two carrier phases of GNSS. The initial phase ambiguities included in the carrier phases are removed by adjusting the relative TEC values derived from pseudoranges. The procedure has been developed by Sori et al. (2019) and Shinbori et al. (2020, 2021). To convert the detrended slant TEC into the vertical TEC, the detrended TEC is multiplied by a slant factor $(1/S(\epsilon))$ which is a ratio of the ionospheric thickness, 200 km, within a height range from 250 to 450 km. Here, S and ϵ are the slant factor and elevation angle of the GNSS satellite. Details of the calculation method have been described in Saito et al. (1998a). For this conversion, we use the slant TEC value of the satellite

zenith angle of less than 75°. Time and spatial resolutions of the grid data are 30 s and $0.25^o \times 0.25^o$ in geographic longitude and latitude, respectively. When we derive the grid data, we calculate the average value with several different detrended TEC ones included in each grid.

We noted that atmospheric perturbations due to Lamb waves triggered by the Tonga volcanic eruption are much faster than cloud motions in the troposphere and calculated the normalized deviation from simple running average of the TIR grid data. The normalized deviation is calculated with the following equations:

$$T_{avg}(t) = \frac{T_{bb}(t+10) + T_{bb}(t) + T_{bb}(t-10)}{3},$$

$$d_3(t) = \frac{T_{bb}(t) - T_{avg}(t)}{T_{avg}(t)},$$

where T_{bb}, t, T_{avg}, and d_3 indicate thermal infrared temperature (K), time (min), simple running average, and normalized deviation from simple running average of the TIR gird data, respectively. In this study, we use the normalized temperature deviation (d_3) of T_{bb} in a comparison with GNSS-TEC and SuperDARN pair of radars observation data. Further, we conduct a 50×50 smoothing for the normalized temperature deviation data to easily identify the wavefront of air pressure disturbances associated with the Tonga volcanic eruption.

In the present study, we also take advantage of several integrated data analysis software, SPEDAS (Angelopoulos et al. 2019) and IUGONET (Hayashi et al. 2013) data analysis software (UDAS; Tanaka et al. 2013).

Results

Figure 1 shows the two-dimensional maps of detrended TEC and normalized temperature deviation in geographic coordinates at 07:00, 08:10, 09:00, and 11:20 UT on 15 January 2022. The blue and purple curves indicate the sunset terminators at a height of 105 and 300 km, corresponding to the E and F region heights, respectively.

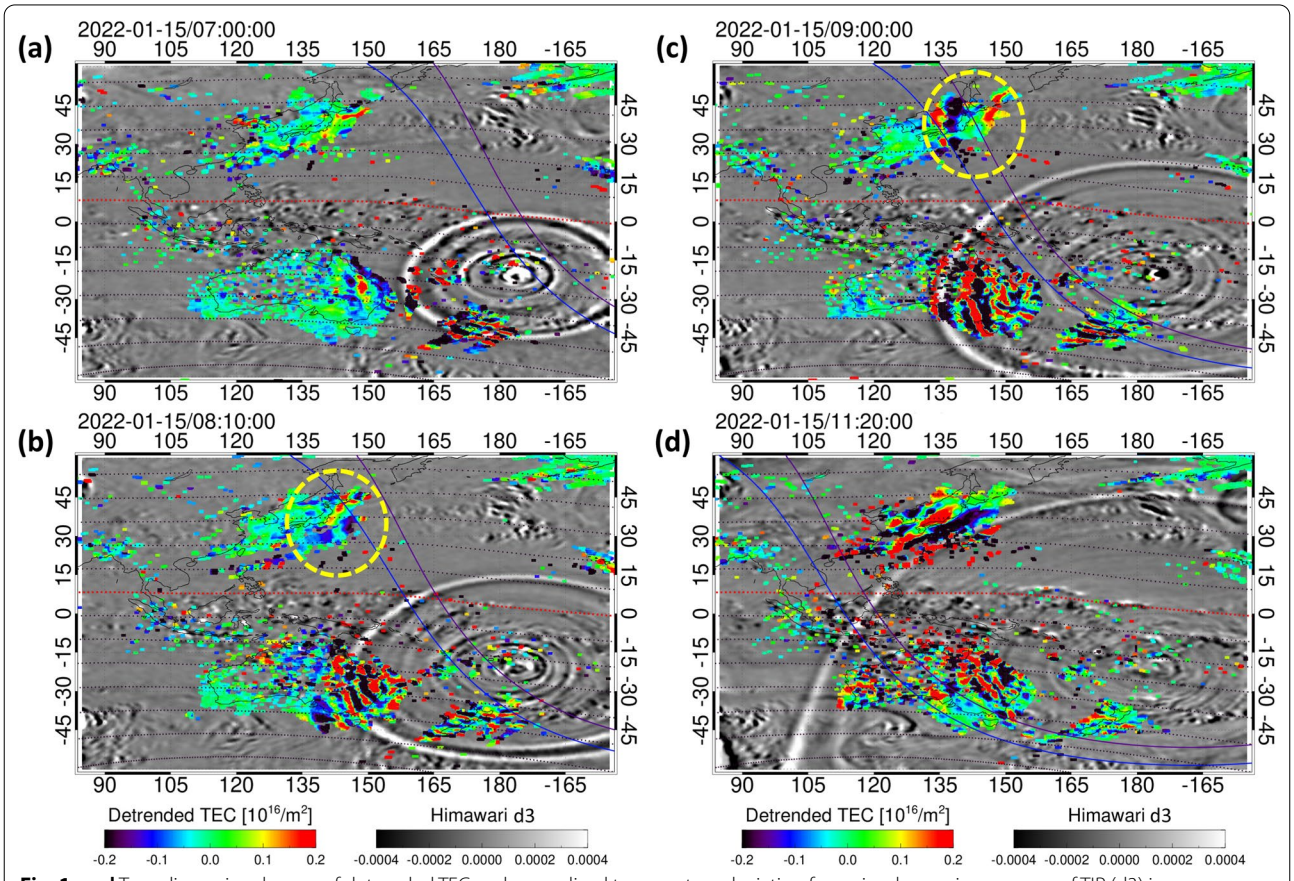

Fig. 1 **a**–**d** Two-dimensional maps of detrended TEC and normalized temperature deviation from simple running average of TIR (d3) in geographical coordinates at 07:00, 08:10, 09:00, and 11:20 UT on 15 January. The d3 value is indicated by the grey scale in a range from −0.0004 to 0.0004. The red horizontal dotted line represents the magnetic equator calculated with the IGRF-13 model. The blue and purple curves indicate the sunset terminators at 105 and 300 km, respectively. The yellow dashed circles in panels (**b**) and (**c**) show that the TEC perturbations appear with a north–south wavefront structure over Japan before the arrival of air pressure disturbances associated with the volcanic eruption

As shown in panels (a)–(d), the concentric wave structure in the normalized temperature deviation associated with the Tonga volcanic eruption extended spatially with time. In panels (b) and (c), the distinct TEC perturbations appeared with several north–south wave structures over Australia. From these maps, the amplitude of the TEC perturbations had more than 0.2 TECU. These wave structures exist almost along the structure of the normalized temperature deviation triggered by air pressure disturbances, which travel at a speed of approximately 320 m/s, corresponding to sound velocity in the troposphere. At 11:20 UT, the air pressure disturbances arrived near Japan, and the TEC perturbations was observed on the north side of the perturbation of normalized temperature deviation. Further, as indicated by the yellow dashed circle in panels (b) and (c), the TEC perturbations appeared with the north–south wave structures over Japan before the arrival of the air pressure disturbances. These wave structures propagated westward with time. Especially, in panel (c), the region where the TEC perturbations were observed over Japan corresponds to the sunset region at a height of the E or F region while the Australian region on the same longitude as that of Japan remained the sunlit region.

Figure 2 shows the two-dimensional maps of detrended TEC and line-of-site Doppler velocity observed by the SuperDARN Hokkaido pair of radars at 08:10 and 09:00 UT plotted with azimuthal equidistant projection. The center latitude and longitude of these maps are 45° and 135°, respectively. To elucidate the characteristics of magnetic conjugacy of the detrended TEC perturbations in both hemispheres, we overplotted the detrended TEC values in the Northern and Southern Hemispheres with the rainbow and gray colors, respectively. In panels (a) and (b), the detrended TEC values indicated by the gray scale color give the detrended TEC ones at the magnetically conjugate points over Japan. That is, most of the detrended TEC values correspond to those over Australia. In panel (b), several spatial distributions of the detrended TEC values in the Northern and Southern Hemispheres were almost consistent with each other. This signature indicates that the TEC perturbations appeared with magnetic conjugacy in both hemispheres. Further, in panel (c), it can be clearly seen that the perturbations of line-of-site Doppler velocity indicated by the pink dashed circle appeared in association with the passage of the TEC perturbations inside a field of view of the SuperDARN Hokkaido east radar. In this case, the positive line-of-site Doppler velocity was observed almost along the wavefront structure of positive TEC perturbations. The Doppler velocity with an amplitude of ~ 50 m/s corresponds to the south-west plasma flow velocity in the ionosphere. This observational fact indicates that the electric field is formed in the perpendicular direction of the wavefront of the TEC perturbations.

In Fig. 2, we showed the magnetic conjugacy of the TEC perturbations observed over Japan and Australia after the Tonga volcanic eruption. To examine whether there is a significant phase difference of the TEC perturbations in between the Northern and Southern Hemispheres, we show the time-series plots of the TEC perturbations at (43.0°N, 140.0°E) and the magnetically conjugate point in Fig. 3. In panel (b), we can identify two distinct TEC perturbations with a large amplitude around 08:40 and 09:20 UT on 15 January 2022, respectively. Corresponding to these phenomena, the TEC perturbations were also observed in the Northern Hemisphere (panel (a)) and a phase difference of the TEC perturbations in between the Northern and Southern Hemispheres was very small. Therefore, this result suggests that the TEC perturbations occur almost simultaneously in both Hemispheres.

In order to investigate the relationship between the perturbations of plasma flow velocity and TEC observed by the Northern and Southern Hemispheres, respectively, we created the range-time plots of (a) line-of-site northward plasma flow velocity, (b) the 15-min high-pass filtered plasma flow velocity, (c) detrended TEC, and (d) normalized temperature deviation along the beam-08 direction of the SuperDARN Hokkaido east radar as shown in Fig. 4. The TEC variation and normalized temperature deviation were observed at the magnetically conjugate points in the Southern Hemisphere. In panel (a), the negative northward plasma flows were observed around 08:10 and 08:50 UT after the arrival of the air pressure disturbances associated with the Tonga volcanic eruption at the magnetically conjugate point of beam-08 in the Southern Hemisphere as shown in panel (d). The period of the plasma flow velocity perturbations was ~ 36–38 min. The onset times varied with dependence on the range gate number of beam-08, indicating that they were delayed with a decreased range gate below the 25 range gates. This time difference seems to correspond to the arrival time of the air pressure disturbances at the locations of each range gate number as shown in panel (e). Further, in panel (b), the 15-min high-pass filtered plasma flow velocity shows the bipolar perturbations with a peak-to-peak amplitude of more than 200 m/s, corresponding to the appearance of large amplitude TEC perturbations at the magnetically conjugate points in the Southern Hemisphere as shown in panel (c). As seen in panels (e) and (f), when the two distinct plasma flow and TEC perturbations with large amplitudes were observed in the Northern and Southern Hemispheres, respectively, the magnetically conjugate points of beam-08 in the Southern Hemisphere belonged to the sunlit region while the observed region of beam-08 in the Northern

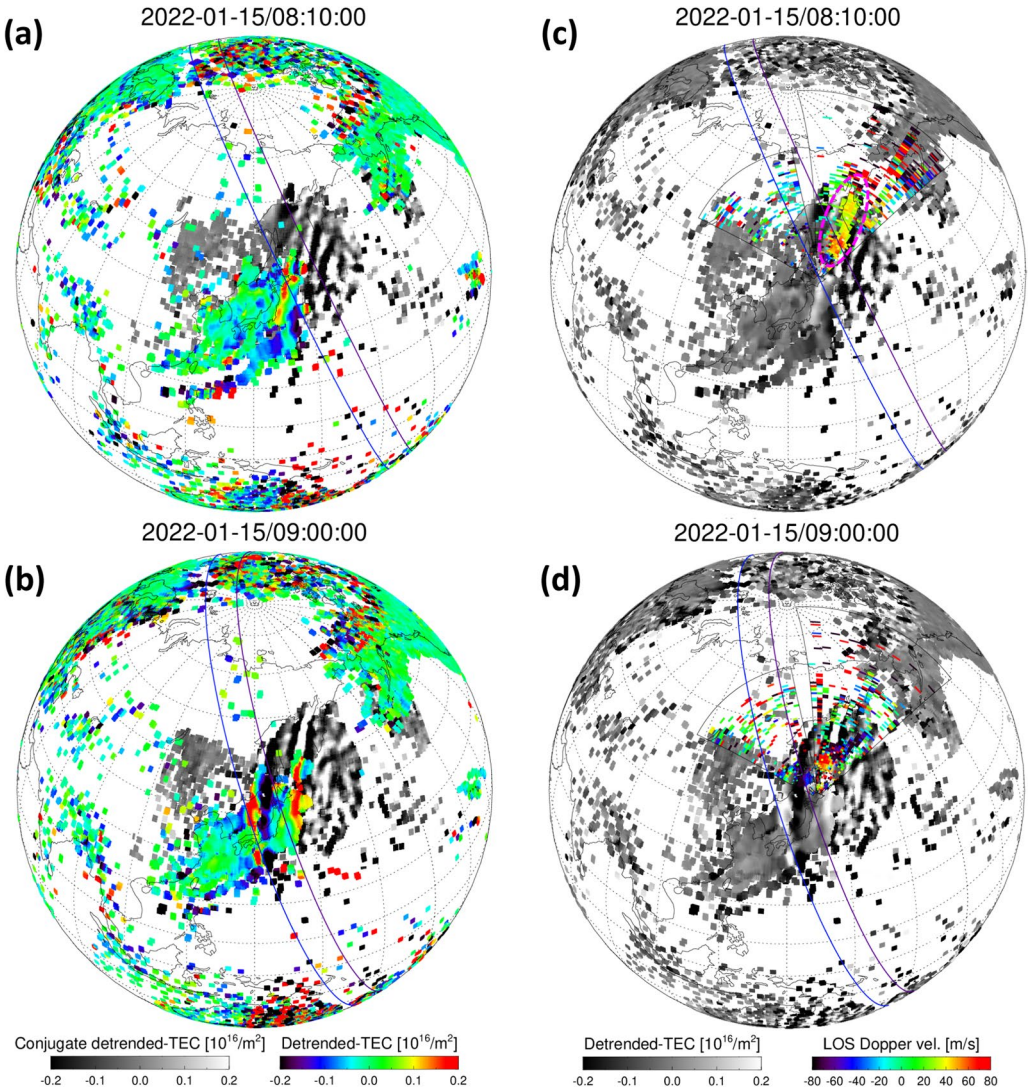

Fig. 2 Polar maps (**a**) and (**b**) of detrended TEC in geographic coordinates at 08:10 and 09:00 UT on 15 January. The detrended TEC values are indicated by two different color codes in a range of −0.2 to 0.2 TECU. The detrended TEC values expressed in the gray scale are the magnetic conjugate detrended TEC ones in the Southern Hemisphere. Polar maps (**c**) and (**d**) of detrended TEC and line-of-site Doppler velocity in geographic coordinates. The plotted time is the same as that of panels (**a**) and (**b**). The line-of-site Doppler velocity observed by the SuperDARN Hokkaido east and west radars is shown by the right-bottom color bar in a range of −80 to 80 m/s. The blue and purple curves show the sunset terminators at a height of 105 and 300 km, respectively. The pink dashed circle in panel (**c**) corresponds to the observed region of positive line-of-site Doppler velocity along the wavefront structure of positive TEC perturbations

Hemisphere already entered the sunset region at a height of the E or F region. This suggests that ionospheric conductivity becomes much smaller in the Northern Hemisphere than in the magnetically conjugate Hemisphere.

Figure 5 shows the time-series plots of (a) line-of-site northward velocity, (b) line-of-site northward velocity mapped onto the Southern Hemisphere along the magnetic field lines and (c) detrended TEC with time interval from 07:50 to 09:50 UT on 15 January 2022. The northward plasma flow velocity in panels (a) and (b) is the 15-min high-pass filtered data. These values are averaged within the number of range gate from 14 to 18. In order to coincide with the time resolution of plasma flow velocity, we conduct a 1-min average of the detrended TEC value. As indicated by the red vertical dashed lines, the time when the TEC perturbations had a peak value does not coincide with that of the peak values of plasma flow velocity. The time difference between the two peak values of the TEC and plasma flow perturbations was 10–12 min. Because the period of the plasma

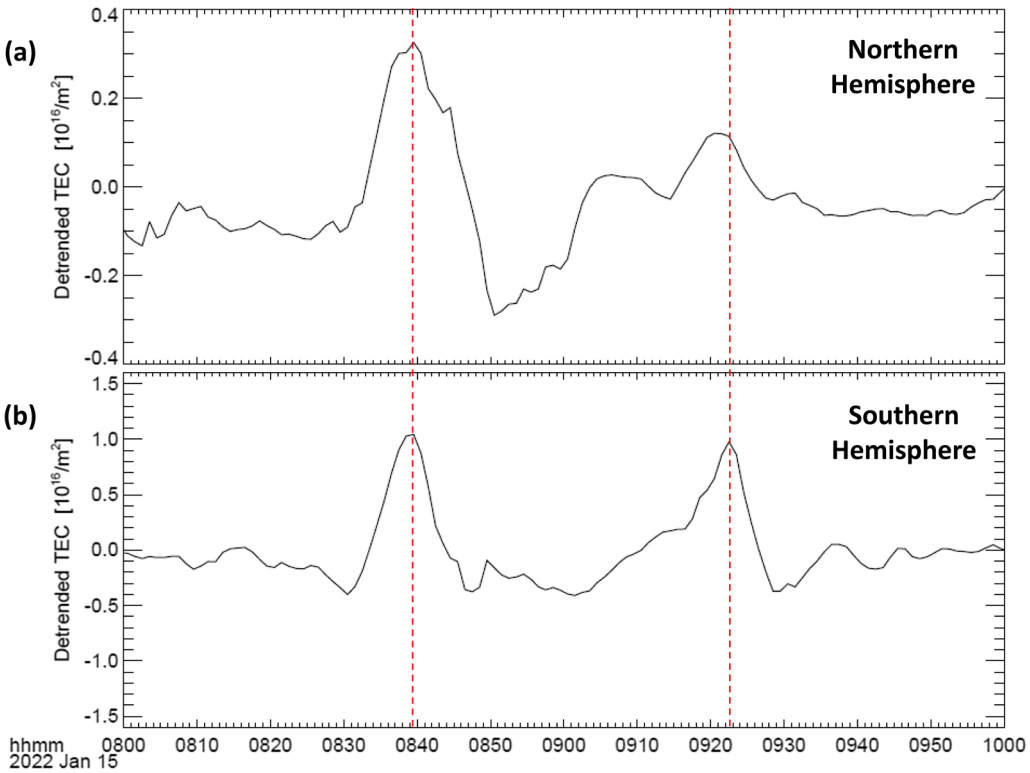

Fig. 3 Time-series plots (**a**) and (**b**) of detrended TEC at (43.0°S, 140.0°E) and the magnetic conjugate point in the Southern Hemisphere. The detrended TEC values are averaged in a latitude range of ±2.0°. The vertical dotted red lines indicate the peak value of detrended TEC at the magnetic conjugate point

flow velocity perturbation with a large amplitude of ~100 m/s was 36–38 min, the zonal electric field perturbations, inducing meridional plasma drift perturbations, coincide with the TEC perturbation with a phase advance of 100°–114°. The physical meaning of the phase difference of the TEC and plasma flow perturbations will be discussed in sections "Physical meaning of a phase difference between the TEC and electric field perturbations in the ionosphere".

Discussion

Influence of geomagnetic storm effects on the ionospheric disturbances

It is unfortunate that a major geomagnetic storm occurred during the Tonga volcanic eruption with a minimum SYM-H value of −101 nT at 22:17 UT on 14 January 2022. Geomagnetic storms are well-known to globally change a spatial distribution of plasma density in the ionosphere and to generate LSTIDs that propagate from high-latitude to low-latitude regions (e.g., Richmond 1978). The signature of LSTIDs is identified as TEC perturbations in two-dimensional maps of detrended TEC (e.g., Tsugawa et al. 2003). Therefore, it is important to investigate influence of geomagnetic storm on the ionospheric disturbances observed during the Tonga volcanic eruption. Figure 6 shows the time-series plots of (a) IMF By, (b) IMF Bz, (c) solar wind proton density, (d) solar wind flow speed, and (e) SYM-H with time interval from 14 to 15 January 2022. In panels (c) and (d), the solar wind flow speed shows a gradual increase from 350 to 580 km/s after a significant enhancement of solar wind proton density from 5 to 20/cc. This signature of solar wind variation is categorized by a CIR phenomenon. Associated with the arrival of the CIR structure, the IMF Bz showed a negative value from 15:00 to 22:45 UT on 14 January, and the amplitude increased until 22:27 UT. The strong southward IMF caused a major geomagnetic storm as shown in the SYM-H variation. The recovery phase of this geomagnetic storm started at 22:21 UT. Because the onset of the Tonga volcanic eruption was around 04:10 UT on 15 January (indicated by the red triangle in panel (e)), based on the Himawari 8 satellite observation, the onset time corresponds to the early recovery phase of the geomagnetic storm. Further, the IMF Bz perturbations became very small during a period from 04:20 to 13:00 UT on 15 January after the Tonga

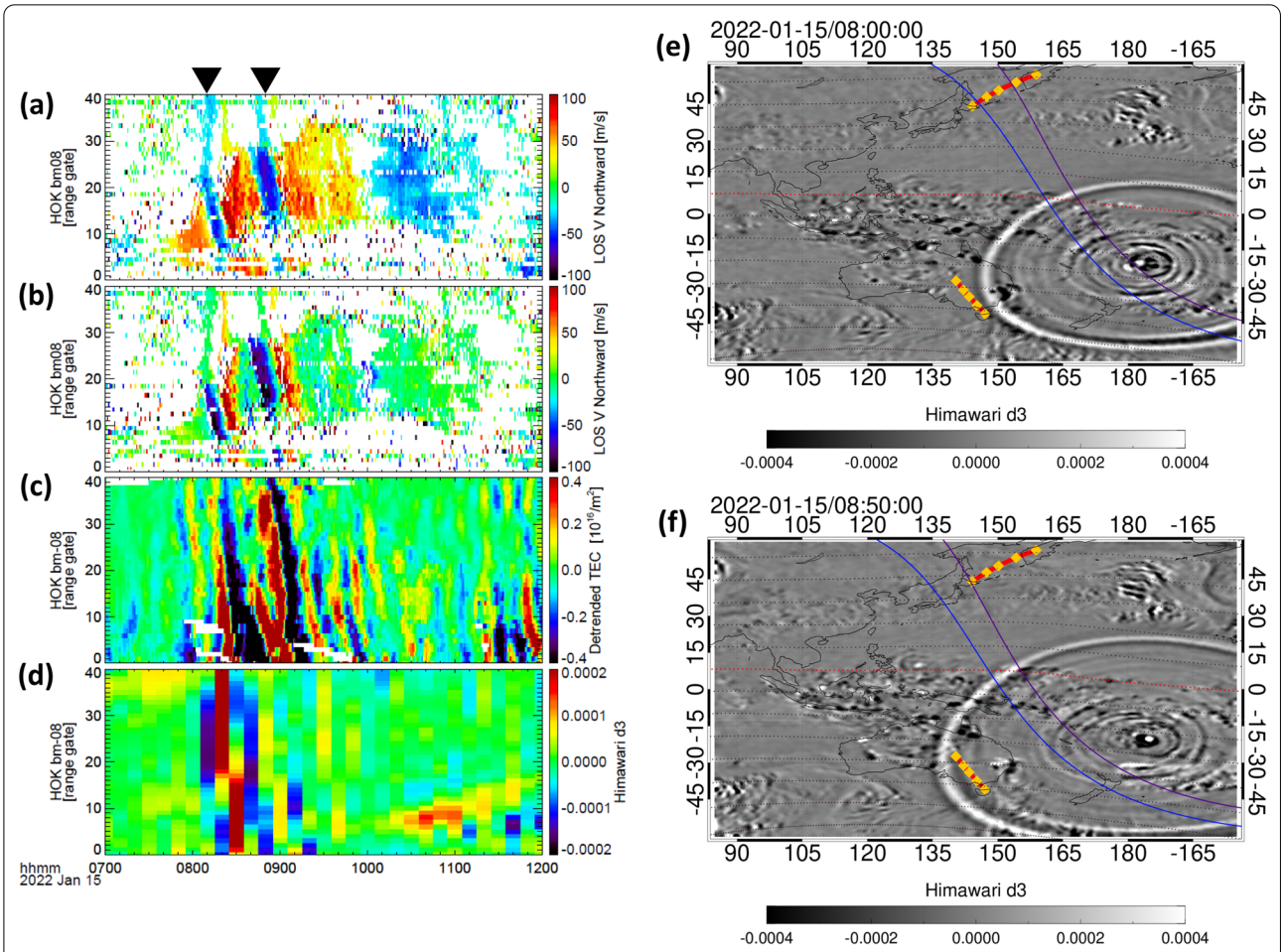

Fig. 4 Range-time plots of **a** northward component of line-of-site plasma velocity, **b** 15-min high-pass filtered plasma velocity, **c** and **d** detrended TEC and normalized temperature deviation (d3) at the magnetic conjugate points of the beam-08 direction in the Southern Hemisphere, **e** and **f** two-dimensional maps of d3 in geographic coordinates. The two red curves with the yellow markers every 10 range gates indicate the locations of line-of-site of beam-08 of the SuperDARN Hokkaido east radar and their magnetic conjugate points in the Southern Hemisphere. The five orange points on these curves indicate the number of range gate from 0 to 40. The two triangles above the left panel correspond to the time of two-dimensional maps of d3. The blue and purple curves in panels (**e**) and (**f**) indicate the sunset terminators at a height of 105 and 300 km, respectively

volcanic eruption. The AE index also showed a low value of less than 200 nT from 04:00 to 11:00 UT on 15 January according to a quick-look plot (http://wdc.kugi.kyoto-u.ac.jp/ae_realtime/202201/index_20220115.html). Therefore, we can consider that an amount of input of solar wind energy to the polar ionosphere was relatively small during this period, and that an influence of this geomagnetic storm on the ionospheric disturbances is almost gone. Actually, we did not find the LSTID signatures propagating equatorward in two-dimensional maps of detrended TEC during the same period, whereas the propagation direction of the TIDs observed with magnetic conjugacy is westward, which is different from that of storm-time LSTIDs (e.g., Tsugawa et al. 2003).

Characteristics of TIDs triggered by the Tonga volcanic eruption

The present study showed that the TEC perturbations with their north–south waveform structure appeared over Japan before the arrival of the air pressure disturbances triggered by the Tonga volcanic eruption. The spatial structure of the TEC perturbations is almost similar to that at the magnetically conjugate points in the Southern Hemisphere (Fig. 2). Further, corresponding to the TEC perturbations, the plasma flow perturbations in the ionosphere were observed by the SuperDARN

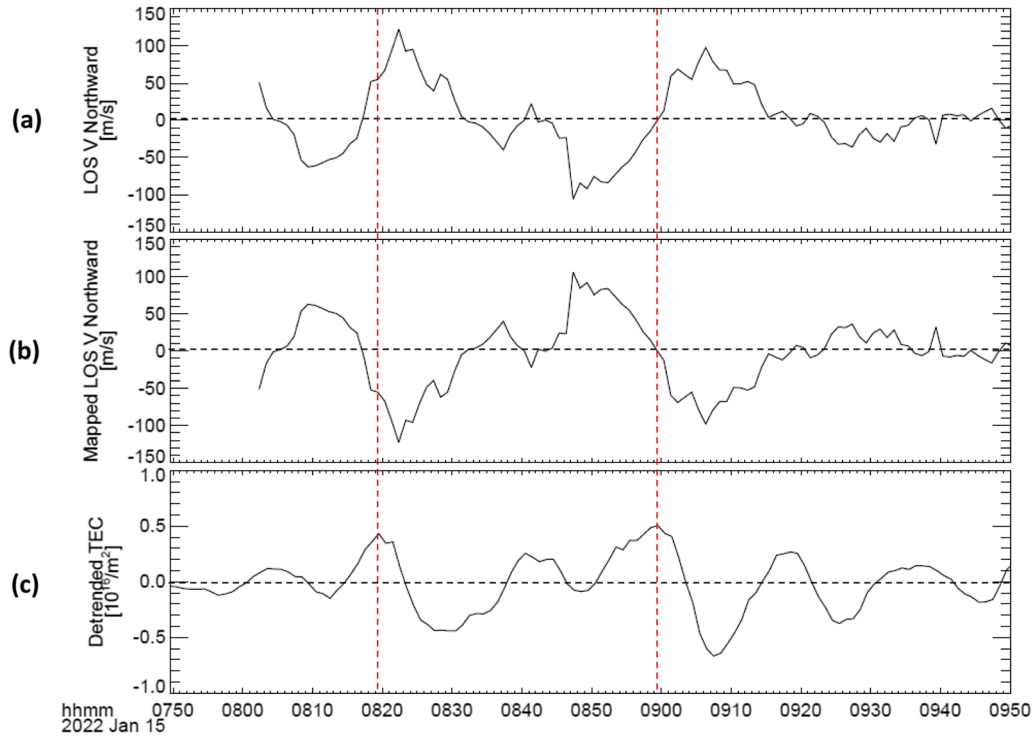

Fig. 5 Time-series plots of **a** line-of-site northward velocity, **b** line-of-site northward velocity mapped onto the Southern Hemisphere, and **c** detrended TEC with time interval from 07:50 to 09:50 UT on 15 January. These values are averaged within the number of range gate from 14 to 18. The two red dotted lines indicate the time of the peak values of two TEC variations with relatively large amplitude

Hokkaido east radar (Figs. 2 and 4). From the plasma flow perturbations, the magnitude of the electric field variations can be estimated as ~2.8–3.1 mV/m. These results imply that the TEC perturbations observed over Japan are not directly generated by atmospheric acoustic waves or AGWs propagating in the neutral atmosphere triggered by the Tonga volcanic eruption, but are driven by the electric field perturbations transmitted along magnetic field lines from the magnetically conjugate points.

Previous studies showed that the 2011 Tohoku earthquake and related tsunami caused the nighttime TIDs with magnetic conjugacy driven by AGWs (e.g., Huba et al. 2015). Huba et al. (2015) studied the ionospheric disturbances associated with tsunami-driven AGWs using the Naval Research Laboratory first-principles ionosphere model SAMI3. They showed that the neutral wind perturbations driven by AGWs lead to plasma flow variations both perpendicular and parallel to magnetic field lines, and that the electric field caused by the neutral wind perturbations propagates to the conjugate hemisphere along the magnetic field lines. Chou et al. (2022) found that the equatorward and westward propagating nighttime MSTIDs appeared over Japan and Australia simultaneously associated with the tsunami oceanic waves. They interpreted that the MSTIDs could be generated by the Perkins instability including the interhemispheric coupling process. Although the above previous studies dealt with the nighttime MSTIDs triggered by the 2011 Tohoku earthquake and related tsunami, the present study analyzed the TEC and plasma flow perturbations in the sunlit Southern and sunset Northern Hemispheres, respectively, at a height of the E region. In this case, because the E-region conductivity in the Northern Hemisphere is much lower than in the Southern Hemisphere, the E-region dynamo field can be generated in the sunlit Southern Hemisphere due to neutral atmospheric oscillation associated with atmospheric acoustic waves and AGWs. Further, the electric field can propagate along the magnetic field lines with a local Alfven velocity and map to the F region in the Northern Hemisphere.

Using Swarm satellite magnetic field, ground GPS-TEC and magnetic field observation data, Aoyama et al. (2016) reported that small-amplitude (~0.5 nT) magnetic field perturbations were observed with magnetic conjugacy in the sunlit region at a height of the E-region approximately 2 h after the first Calbuco volcanic eruption in southern Chile on 22 April 2015. They also found that the observed period of magnetic field perturbations was almost consistent with that of the TEC perturbations. From these observational

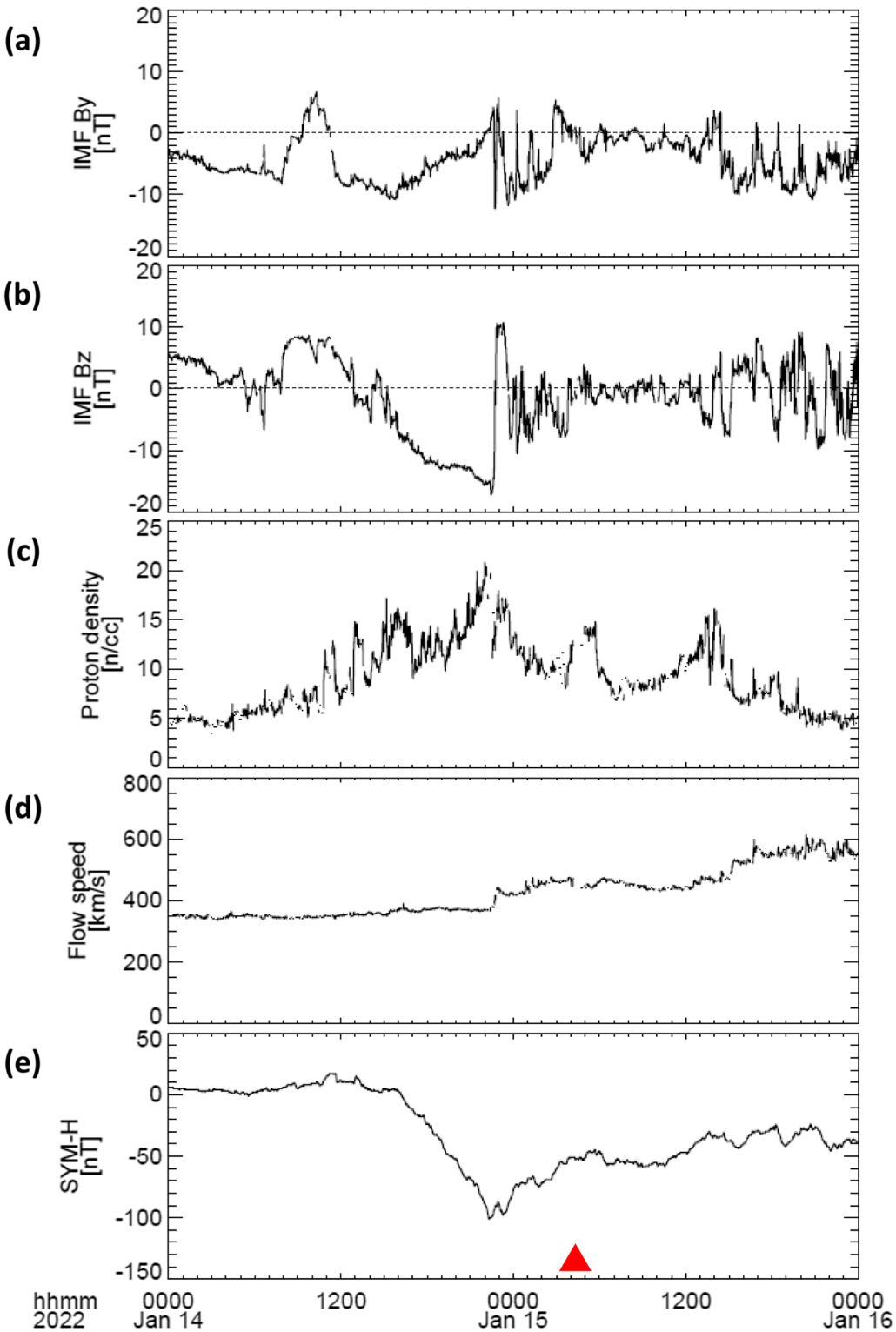

Fig. 6 Time-series plots of **a** IMF By, **b** IMF Bz, **c** solar wind proton density, **d** solar wind flow speed, and **e** SYM-H with time interval from 14 to 15 January 2022. The red triangle indicates the onset time of the Tonga volcanic eruption

facts, Aoyama et al. (2016) interpreted that the small-amplitude magnetic field perturbations are produced by small-scale field-aligned currents due to divergence of E-region dynamo currents flowing in the horizontal direction. According to Fig. 1 found in Aoyama et al. (2016), it is shown that a source of the E-region dynamo currents is the neutral wind oscillation due to AGWs triggered by a volcanic eruption. Such small-amplitude magnetic field perturbations are always observed with magnetic conjugacy in the topside ionosphere except for volcanic eruptions (Nakanishi et al. 2014).

Based on the above discussion, we can infer that the TEC perturbations with magnetic conjugacy after the Tonga volcanic eruption can be driven by the electric field perturbations generated by the E-region dynamo in the sunlit Southern Hemisphere, where the E and F regions of the ionosphere are also directly modulated by upward propagation of atmospheric acoustic waves and AGWs (e.g., Themens et al. 2022). In Figs. 2 and 5, the present study showed that there is no significant phase difference of the two distinct TEC perturbations in between the Northern and Southern Hemispheres around 08:10 and 09:00 UT, but that the phase difference of 10−12 min exists between the TEC and electric field perturbations. As will be shown in sections "Physical meaning of a phase difference between the TEC and electric field perturbations in the ionosphere", this result suggests observational evidence that the TEC perturbations in both hemispheres are driven by the external electric field. Therefore, it can be thought that these two distinct TEC perturbations are more dominantly generated by the E-region dynamo electric field than by direct modulation of the ionosphere due to upward propagation of atmospheric acoustic waves and AGWs. On the other hand, in Fig. 1d, it was shown that the spatial structure of the TEC perturbations was different between the sunset Northern and Southern Hemispheres. For example, the TEC perturbations aligned with a wavefront of the air pressure waves over Japan had no magnetic conjugacy with those over Australia. In this case, because ionospheric Pedersen and Hall conductivities in this region are very small (Σ_P: 0.2 S, Σ_H: 0.1 S) (they are calculated with an IDL software package (Koyama et al. 2014)), it can be considered that the E-region dynamo process does not work enough to generate the electric field that drives the TEC perturbations. Therefore, the TEC perturbations with no magnetic conjugacy can be mainly driven by ionospheric modulation triggered by upward propagation of atmospheric acoustic waves and AGWs. Based on this discussion, it can be considered that ionospheric conductivity is one of the important parameters for generation of the E-region dynamo electric field and related TIDs. This point should be solved by atmosphere–ionosphere coupling model in future study.

Here, we discuss the short-circuited effect of the E-region dynamo field on mapping the electric field to the sunset Northern Hemisphere due to high conductivities in the sunlit ionosphere. Figure 7 shows an equivalent electric circuit of magnetosphere/plasmasphere–ionosphere current system connecting between the sunlit Southern Hemisphere and the sunset Northern Hemisphere. As seen in this figure, the dynamo layer is located in a height range from 80 to 130 km in the sunlit ionosphere (e.g., Shinbori et al. 2010), where the Hall conductivity is dominant, and the dynamo current is concentrated. The dynamo current produced by neutral atmospheric oscillation due to atmospheric acoustic waves and AGWs is estimated as:.

$$I_x^{dyn} = \int_{80}^{130} j_x^{dyn} dz = U_{xd}^n B \int_{80}^{130} \sigma_H dz = \Sigma_H U_{xd}^n B,$$

where Σ_H is a height-integrated Hall conductivity of the dynamo layer, and U_{xd}^n is a neutral particle velocity in the dynamo layer associated with atmospheric acoustic waves and AGWs. The dynamo current I_x^{dyn} is partially shunted by a Pedersen current ($j_{cx} = \sigma_P E_x$) and is partially closed by a parallel current I_z flowing along the magnetic field lines. The parallel current is closed by a Pedersen current ($j_{cx} = \sigma_p^{'} E_x$) flowing in the magnetically conjugate ionosphere as shown in Fig. 7. The effective transverse current (I_x) (dynamo current minus Pedersen current) is

$$I_x = I_x^{dyn} - I_x^c = \frac{\Sigma_P^{'} \Sigma_H}{\Sigma_P + \Sigma_P^{'}} U_{xd}^n B.$$

The zonal electric field due to a voltage drop when current flows through the current circuit (Fig. 7) becomes

$$E_x = \frac{\Sigma_H}{\Sigma_P + \Sigma_P^{'}} U_{xd}^n B.$$

This electric field propagates along the magnetic field lines and is mapped to both the F region in the Southern Hemisphere and magnetically conjugate ionosphere in the Northern Hemisphere as indicated by the red arrows in Fig. 7. From the above equation, the value of the mapped electric field depends on both the integrated conductivities (Σ_H and Σ_P) around current generator and on the condition of the electric circuit closing the conjugate ionosphere. For example, in a case of $\Sigma_P^{'} \rightarrow 0$, the magnetic field variation is absent, and the electric field variation becomes maximum. When we calculate the realistic ionospheric Hall and Pedersen conductivities at (50.36°N, 149.20°E) and the magnetically conjugate point (33.52 °S, 143.26

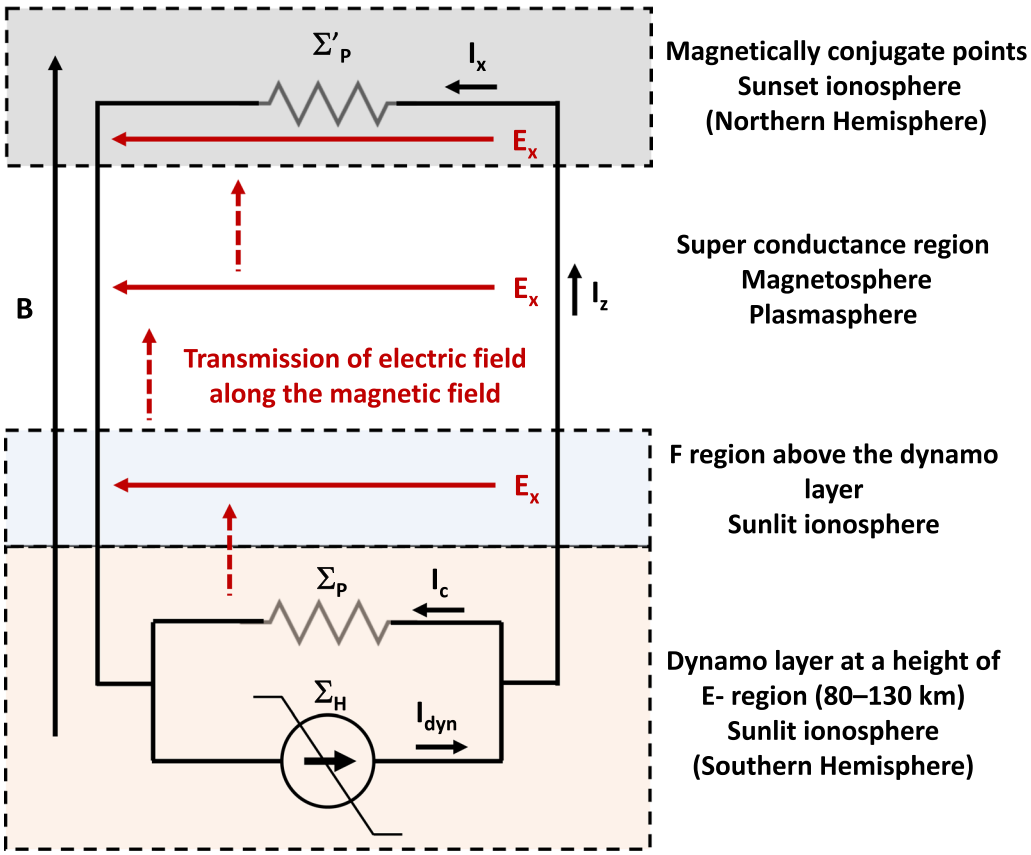

Fig. 7 Equivalent electric circuit of magnetosphere–ionosphere current system connecting between the sunlit Southern Hemisphere and the sunset Northern Hemisphere. The red arrows indicate the dynamo electric field mapped in the F region of the ionosphere and in the magnetically conjugate ionosphere

°E) at 08:10 UT on 15 January 2022 with an IDL software package (Koyama et al. 2014), the Σ_H, Σ_P, and $\Sigma_P^{'}$ values become 6.8 S, 5.5 S, and 0.58 S, respectively. Therefore, the relationship between the zonal electric field E_x and the dynamo field $U_{xd}^n B$ is

$$E_x = 1.1 U_{xd}^n B.$$

This result indicates that an E-region dynamo field generated by neutral atmospheric oscillation due to atmospheric acoustic waves and AGWs triggered by the Tonga volcanic eruption can be mapped to the magnetically conjugate ionosphere even if there exists a shunted effect of the dynamo current on the high conductivity in the daytime F region. Further, from the SuperDARN radar observation and IGRF-13 model data, we can estimate the neutral wind oscillation due to atmospheric acoustic waves and AGWs in the sunlit Southern Hemisphere (33.52°S, 143.26°E) as ~ 46–51 m/s.

Physical meaning of a phase difference between the TEC and electric field perturbations in the ionosphere

Our observations showed that the TEC perturbations caused by the Tonga volcanic eruption are accompanied by electric field perturbations and that the zonal electric field perturbation, inducing the meridional plasma drift perturbation, coincides with the TEC perturbation with a phase advance of 100°–114°. Nighttime MSTIDs with a wavefront elongating from northwest to southeast in the Northern Hemisphere (from southwest to northeast in the Southern Hemisphere), which are frequently observed at middle latitudes, are also accompanied by oscillating electric fields (Saito et al. 1998b; Shiokawa et al. 2003). An increase (decrease) in electron density caused by the nighttime MSTIDs coincides with the eastward (westward) component of the electric fields (Shiokawa et al. 2003; Otsuka et al. 2007). This result indicates that the electric fields in the nighttime MSTIDs are generated to maintain the current continuity which flows

in the F region in the Northern Hemisphere (southeastward in the Southern Hemisphere). A fact that the phase relationship between the electron density and electric field for the TIDs after the Tonga volcanic eruption is different from that for the nighttime MSTIDs suggests the difference of mechanism generating TIDs. When the TID appeared for the first time over Australia, the ionosphere embedding the TIDs is located at the sunlit. Therefore, an electric field in the ionosphere could be generated mainly in the E region. Even if an electric field is generated by an F region dynamo due to the neutral wind oscillation associated with atmospheric acoustic waves and AGWs, the electric field is short-circuited thorough the highly conductive E region. Consequently, the TIDs after the Tonga eruption could be generated by the electric field perturbations driven by the E-region dynamo in the Southern Hemisphere.

To test this hypothesis, we have carried out a simple model calculation of the electron density for the case that an external oscillating electric field exists. According to Shiokawa et al. (2003) and Otsuka et al. (2013), from the continuity equation for the ions, the electron density perturbation n_{e1} caused by oscillating ion velocity v_1 perpendicular to the geomagnetic field is obtained as follows:

$$n_{e1} = -\frac{i}{\omega} v_1 \frac{\partial n_e}{\partial z} \cos I,$$

where $i = \sqrt{-1}$, ω is an angular frequency of MSTIDs, I is a dip angle of the geomagnetic field, n_e is a background electron density, z is altitude. To derive this equation, perturbed quantities n_{e1} and v_1 are assumed to be a plane wave $n_{e1}, v_1 \propto exp\{i(\omega t - kx)\}$, where t is time, k is a wave number, and x is a horizontal distance. Due to the ion motion at velocity of v_1 which is caused by $\mathbf{E} \times \mathbf{B}$ drift due to the E-region dynamo electric fields, the F region is uplifted and pushed down. The vertical displacement of $\frac{\partial n_e}{\partial z}$ is responsible for the electron density perturbation n_{e1}. The amplitude of n_{e1} is proportional to the vertical component of the $\mathbf{E} \times \mathbf{B}$ drift, that is, $v_1 \cos I$.

Figure 8a shows the calculated electron density as a function of time and altitude for the case that v_1 oscillates with a period of 36 min and amplitude of 100 m/s. These period and amplitude of v_1 is determined based on the observation of the ion velocity by the SuperDARN Hokkaido east radar, respectively. The background electron density is taken from the IRI-2016 model (Bilitza et al. 2017; Bilitza 2018) to reproduce the ionosphere at (32.4°S, 142.7°E) on January 2022 with $F_{10.7}$ (Tapping 2013) equal to 115, The background vertical TEC, which is an integration of the electron density over an altitude range from 150 to 600 km in Fig. 8a, is 16.1 TECU, which is consistent with the TEC on this night. The TEC perturbation is shown in Fig. 5b. The amplitude of the TEC

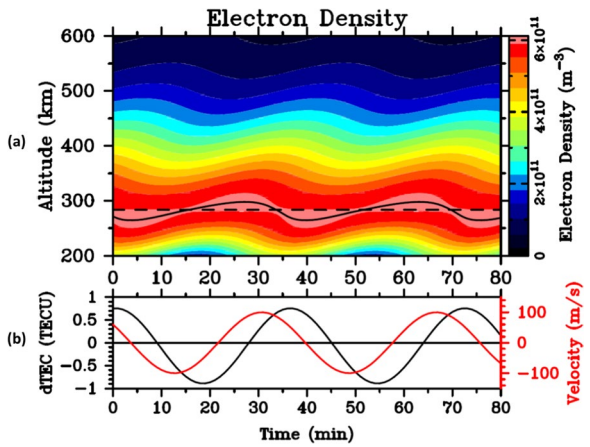

Fig. 8 **a** Model calculation of electron density in the F region for the case the electric field oscillating with a period of 36 min and amplitude of 100 m/s for $\mathbf{E} \times \mathbf{B}$ drift. Solid line and dotted line indicate peak altitude of electron density and original peak altitude of electron density without electric field oscillation, respectively. **b** Temporal variation of TEC (black) and plasma drift velocity (red) perturbations. TEC is an integration of the electron density from 200 to 600 km in altitude

perturbation is approximately 0.7 TECU. This amplitude is also consistent with the GNSS-TEC observation. In Fig. 8b, it is found that a phase of v_1 is approximately 90° (7 min) earlier than that of the TEC perturbation, and that the observed phase relationship between the plasma drift velocity perturbation and TEC perturbation is well reproduced. The result obtained from the model calculation suggests that the TIDs after the Tonga volcanic eruption are caused by the perturbed electric field generated in a place different from the F region of the ionosphere.

Scenario of TEC and electric field perturbations in the ionosphere triggered by the Tonga volcanic eruption

On the basis of the above discussion in sub sections "Characteristics of TIDs triggered by the Tonga volcanic eruption" and "Physical meaning of a phase difference between the TEC and electric field perturbations in the ionosphere", we can depict a schematic view of scenario of TEC and electric field perturbations in the ionosphere triggered by the Tonga volcanic eruption as seen in GNSS-TEC and SuperDARN Hokkaido pair of radars observations as shown in Fig. 9. In this scenario, we deal with two distinctive TEC and electric field perturbations with the large amplitude at 08:10 and 09:00 UT shown in Fig. 4. Associated with the Tonga volcanic eruption, atmospheric acoustic waves and AGWs are generated by air pressure disturbances and propagate in the lower atmosphere and thermosphere. The neutral wind oscillation triggered by these atmospheric disturbances

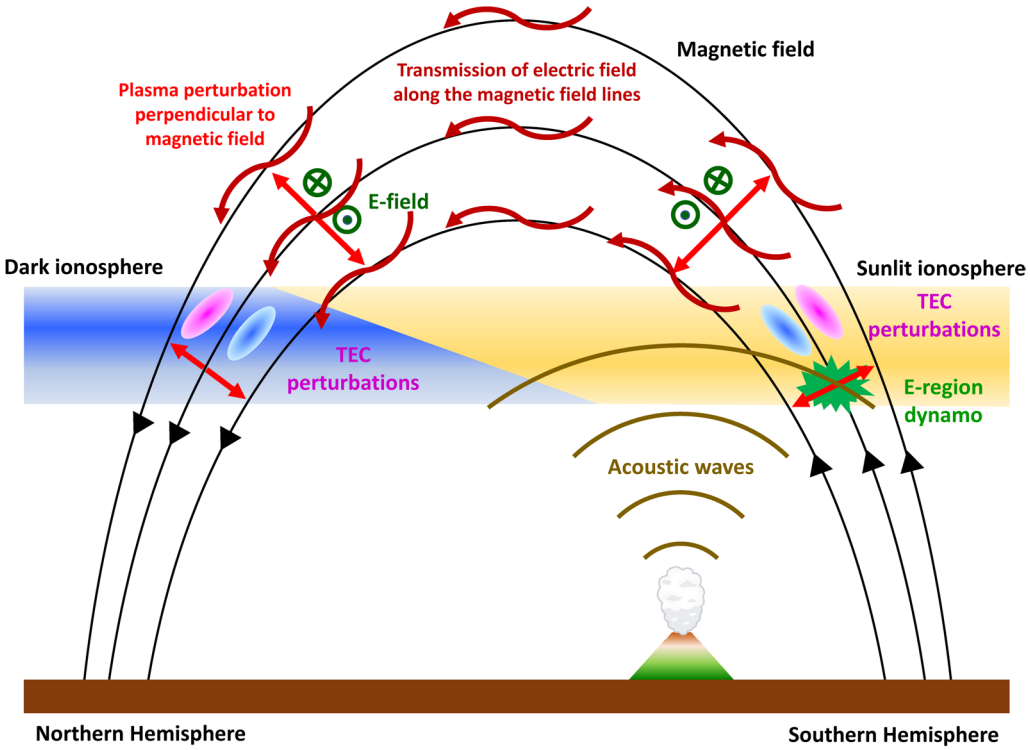

Fig. 9 A schematic view of scenario of TEC and electric field perturbations in the ionosphere triggered by the Tonga volcanic eruption as seen in GNSS-TEC and SuperDARN radar observations. The red arrows perpendicular to magnetic field lines indicate the plasma flow variations driven by the eastward and westward electric fields. The pink and blue circles represent the positive and negative TEC perturbations, respectively

drives an E-region dynamo in the sunlit region through the interaction between the charged and neutral particles and the dynamo electric field is transmitted to the F region in both hemispheres along the magnetic field lines. The propagation speed corresponds to a local Alfven speed depending on the magnetic field intensity and plasma density, which is much faster than that of atmospheric acoustic waves and AGWs. The dynamo field leads to the TEC and plasma flow perturbations in the F region in both hemispheres. In this case, because the electric field is an external field, there is a phase difference between the TEC and plasma flow perturbations as shown in Figs. 5 and 8.

Conclusions

To elucidate the characteristics of electromagnetic conjugacy of TIDs observed in both Northern and Southern Hemispheres just after the 15 January 2022 Hunga Tonga-Hunga Ha'apai volcanic eruption and the generation mechanism, we analyze GNSS-TEC data derived from ~7200 globally distributed GNSS stations and ionospheric plasma velocity data obtained from the SuperDARN Hokkaido pair of radars. Further, we use TIR grid data with high spatial resolution observed by the Himawari 8 satellite to investigate lower atmospheric disturbances associated with surface air pressure waves propagating as a Lamb mode. After 07:30 UT on 15 January, two distinct TIDs propagating in the westward direction appeared in the Japanese sector with almost the same structure as those at the magnetically conjugate points in the Southern Hemisphere. Corresponding to these two distinct TIDs with their large amplitude of 0.5–1.1 TECU observed in the Southern Hemisphere, the plasma flow direction in the F region changed from southward to northward. At this time, the magnetically conjugate points in the Southern Hemisphere were located in the sunlit E region. The amplitude and period of the plasma flow variation were ~100–110 m/s and ~36–38 min, respectively. From the plasma flow perturbation, a zonal electric field can be estimated as ~2.8–3.1 mV/m. Further, there was a significant phase difference of ~10–12 min between the TEC and plasma flow perturbations. The existence of a phase difference between the TEC and plasma flow perturbations could also be verified by a simple model calculation of the electron density for the case that an external oscillating electric field exists. These results suggest that an E-region dynamo electric field driven by the neutral wind oscillation associated

with atmospheric acoustic waves and AGWs propagates to the F region and the magnetically conjugate ionosphere along magnetic field lines with a local Alfven speed. The propagation speed is much faster than that of Lamb mode waves. As a result, the electric field generates ionospheric disturbances in both hemispheres with no significant phase difference before the air pressure disturbances related to the Tonga volcanic eruption arrive in Japan. Therefore, it can be concluded that the generation mechanism of the two distinct TIDs triggered by the Tonga volcanic eruption is different from that of normal nighttime MSTIDs.

Abbreviations

AE: Auroral electrojet; AGW: Atmospheric gravity wave; CDAWeb: Coordinated data analysis web; CEReS: Center for Environmental Remote Sensing; CIR: Corotating interaction region; EUV: Extreme ultraviolet; GSM: Geocentric solar magnetic; GNSS: Global Navigation Satellite System; IDL: Interactive data language; IGRF-13: 13Th International Geomagnetic Reference Field; IMF: Interplanetary magnetic field; IRI: International reference ionosphere; IUGONET: Inter-University Upper Atmosphere Observation Network; LSTID: Large-scale traveling ionospheric disturbance; MSTID: Medium-scale traveling ionospheric disturbance; NASA: National Aeronautics and Space Administration; RW: Rayleigh wave; SAMI3: Sami3 is a model of the ionosphere; SPEDAS: Space Physics Environment Data Analysis System; SuperDARN: Super Dual Auroral Radar Network; SYM-H: Horizontal SYMmetric disturbance; TEC: Total electron content; TECU: TEC unit (TECU = 10^{16} el/m^2); TID: Traveling ionospheric disturbance; TIR: Thermal InfRared; UDAS: IUgonet data analysis software; UT: Universal time; VEI: Volcanic Explosivity Index.

Acknowledgements

This work was supported by a JSPS KAKENHI Grant nos. 16H06286, 18KK0099, 22H01284, 20H00197, 21H04518, JSPS Bilateral Joint Research Projects no. JPJSBP120226504, and JSPS Core-to-Core Program, B. Asia-Africa Science Platforms. The coauthor (Nozomu Nishitani) was supported by a JSPS KAKENHI Grant nos. 18KK0099, 21H04518, and 22H01284. The coauthor (Takuo Tsuda) was supported by a JSPS KAKENHI Grant no. JP21H01144. We used the IUGONET database (IUGONET Type-A) and data analysis software (UDAS). The GNSS data collection and processing were performed using the NICT Science Cloud. Himawari 8 gridded data are distributed by the CEReS, Chiba University, Japan. SuperDARN is a collection of radars funded by the national scientific funding agencies of Australia, Canada, China, France, Italy, Japan, Norway, South Africa, United Kingdom, and the United States of America.

Author contributions

AS carried out a major part of data analysis and wrote the manuscript. YO provided numerical simulation results and wrote the sentences in Section "Physical meaning of a phase difference between the TEC and electric field perturbations in the ionosphere". TT calculated the normalized deviation from simply running average (d3) of Himawari 8 TIR grid data. TS, PS, MN, and NN participated in reviewing the paper. All authors read and approved the final manuscript.

Funding

This work was supported by a JSPS KAKENHI Grant Nos. 16H06286, 18KK0099, 22H01284, 20H00197, 21H04518, JSPS Bilateral Joint Research Projects no. JPJSBP120226504, and JSPS Core-to-Core Program, B. Asia-Africa Science Platforms. The coauthor (Nozomu Nishitani) was supported by a JSPS KAKENHI Grant Nos. 18KK0099, 21H04518, and 22H01284. The coauthor (Takuo Tsuda) was supported by a JSPS KAKENHI Grant No. JP21H01144.

Availability of data and materials

The solar wind, IMF data were provided by provided by the NASA CDAWeb (https://cdaweb.sci.gsfc.nasa.gov/index.html/). We used geomagnetic index (AE and SYM-H) with 1-min time resolution provided by the World Data Center for Geomagnetism, Kyoto University (http://wdc.kugi.kyoto-u.ac.jp/index.html). The Receiver Independent Exchange Format data used for GNSS-TEC processing were provided by 50 data providers. These have been listed on the webpage of the GNSS-TEC database (http://stdb2.isee.nagoya-u.ac.jp/GPS/GPS-TEC/gnss_provider_list.html). The mainly contributed providers are UNAVCO (https://www.unavco.org/data/gps-gnss/gps-gnss.html), CDDIS (https://cddis.nasa.gov/archive/gnss/data/daily/, Noll, 2010), CHAIN (http://chain.physics.unb.ca/chain/pages/data_download, Jayachandran et al. 2009), PNGA (http://www.geodesy.cwu.edu, Pacific Northwest Geodetic Array (PANGA), 1996), IBGE (http://geoftp.ibge.gov.br/informacoes_sobre_posicionamento_geodesico/rbmc/dados/), SOPAC (http://garner.ucsd.edu/pub/rinex/), GEONET (http://datahouse1.gsi.go.jp/terras/terras_english.html), GNNZ (https://www.geonet.org.nz/data/types/geodetic), RENAG (https://doi.org/10.15778/resif.rg, RESIF, 2017), SONEL (https://www.sonel.org/-GPS-.html), LINZ (https://apps.linz.govt.nz/ftp/positionz), INGV (http://ring.gm.ingv.it/, INGV RING Working Group, 2016), SWSBM (https://www.sws.bom.gov.au/World_Data_Centre/1/1), AFREF (http://afrefdata.org/), TLALOCNET (http://tlalocnet.udg.mx/tlalocnetgsac/), Northern California Earthquake Data Center (NCEDC, 2014; https://ncedc.org/bard.overview.html), EUREF (https://www.epncb.oma.be/, Bruyninx et al. 2019), RAMSAC (https://www.ign.gob.ar/NuestrasActividades/Geodesia/Ramsac/DescargaRinex, Piñón et al. 2018), and BIGF (http://www.bigf.ac.uk/data_access.html). The common time SuperDARN data in CDF format (Hori et al. 2013) at HKW and HOK were obtained from the ERG Science Center operated by ISAS/JAXA and ISEE/Nagoya University (https://ergsc.isee.nagoya-u.ac.jp/index.shtml.en, Miyoshi et al. 2018). The Himawari 8 satellite TIR grid data are provided by the CEReS, Chiba University (http://www.cr.chiba-u.jp/databases/GEO/H8_9/FD/index_en_V20190123.html). The F10.7 index was provided by Natural Resources Canada (https://spaceweather.gc.ca/forecast-prevision/solar-solaire/solarflux/sx-5-flux-en.php).

Declarations

Ethics approval and consent to participate

Not applicable.

Consent for publication

Not applicable.

Competing interests

The authors declare that they have no competing interests.

Author details

[1]Institute for Space-Earth Environmental Research (ISEE), Nagoya University, Nagoya, Aichi 464-8601, Japan. [2]National Institute of Information and Communications Technology (NICT), Koganei, Tokyo 184-8795, Japan. [3]The University of Electro-Communications, Chofugaoka, Chofu, Tokyo 182-8585, Japan.

Received: 15 March 2022 Accepted: 15 June 2022
Published online: 13 July 2022

References

Adam D (2022) Tonga volcano eruption created puzzling ripples in Earth's atmosphere. Nature 601:497. https://doi.org/10.1038/d41586-022-00127-1

Alken P, Thébault E, Beggan CD, Amit H, Aubert J, Baerenzung J, Bondar TN, Brown WJ, Califf S, Chambodut A, Chulliat A, Cox GA, Finlay CC, Fournier A, Gillet N, Grayver A, Hammer MD, Holschneider M, Huder L, Hulot G, Jager T, Kloss C, Korte M, Kuang W, Kuvshinov A, Langlais B, Léger J-M, Lesur V, Livermore PW, Lowes FJ, Macmillan S, Magnes W, Mandea M, Marsal S, Matzka J, Metman MC, Minami T, Morschhauser A, Mound JE, Nair M, Nakano S, Olsen N, Pavón-Carrasco FJ, Petrov VG, Ropp G, Rother M, Sabaka TJ, Sanchez S, Saturnino D, Schnepf NR, Shen X, Stolle C, Tangborn A, Tøffner-Clausen L, Toh H, Torta JM, Varner J, Vervelidou F, Vigneron P, Wardinski I, Wicht J, Woods A, Yang Y, Zeren Z, Zhou B (2021) International geomagnetic reference field: the thirteenth generation. Earth Planet Space 73:49. https://doi.org/10.1186/s40623-020-01288-x

Ajith KK, Li G, Tulasi Ram S, Yamamoto M, Hozumi K, Abadi P, Xie H (2020) On the seeding of periodic equatorial plasma bubbles by gravity

waves associated with tropical cyclone: a case study. J Geophys Res 125:e2020JA028003. https://doi.org/10.1029/2020JA028003
Angelopoulos V et al (2019) The space physics environment data analysis system (SPEDAS). Space Sci Rev. https://doi.org/10.1007/s11214-018-0576-4
Aoyama T, Iyemori T, Nakanishi K, Nishioka M, Rosales D, Veliz O, Safor EV (2016) Localized field-aligned currents and 4-min TEC and ground magnetic oscillations during the 2015 eruption of Chile's Calbuco volcano. Earth Planet Space 68:148. https://doi.org/10.1186/s40623-016-0523-0
Astafyeva E (2019) Ionospheric detection of natural hazards. Rev Geophys 57:1265–1288. https://doi.org/10.1029/2019RG000668
Astafyeva E, Maletckii B, Mikesell TD, Munaibari E, Ravanelli M, Coisson P, Manta F, Rolland L (2022) The 15 January 2022 Hunga Tonga eruption history as inferred from ionospheric observations. Geophys Res Lett 49:e2022GL098827. https://doi.org/10.1029/2022GL098827
Bilitza D (2018) IRI the international standard for the ionosphere. Adv Radio Sci 16:1–11. https://doi.org/10.5194/ars-16-1-2018
Bilitza D, Altadill D, Truhlik V, Shubin V, Galkin I, Reinisch B, Huang X (2017) International reference ionosphere 2016: from ionospheric climate to real-time weather predictions. Space Weather 15:418–429. https://doi.org/10.1002/2016SW001593
Bruyninx C, Legrand J, Fabian A, Pottiaux E (2019) GNSS metadata and data validation in the EUREF permanent network. GPS Solut 23:106. https://doi.org/10.1007/s10291-019-0880-9
Carr JL, Horváth Á, Wu DL, Friberg MD (2022) Stereo plume height and motion retrievals for the record-setting Hunga Tonga-Hunga Ha'apai eruption of 15 January 2022. Geophys Res Lett 49:e2022GL098131. https://doi.org/10.1029/2022GL098131
Carvajal M, Sepúlveda I, Gubler A, Garreaud R (2022) Worldwide signature of the 2022 Tonga volcanic tsunami. Geophys Res Lett 49:e2022GL098153. https://doi.org/10.1029/2022GL098153
Choosakul N, Saito A, Iyemori T, Hashizume M (2009) Excitation of 4-min periodic ionospheric variations following the great Sumatra-Andaman earthquake in 2004. J Geophys Res 114:A10313. https://doi.org/10.1029/2008JA013915
Chou MY, Lin CH, Yue J, Chang LC, Tsai HF, Chen CH (2017) Medium-scale traveling ionospheric disturbances triggered by Super Typhoon Nepartak (2016). Geophys Res Lett 44:7569–7577. https://doi.org/10.1002/2017GL073961
Chou MY, Yue J, Lin CCH, Rajesh PK, Pedatella NM (2022) Conjugate effect of the 2011 Tohoku reflected tsunami-driven gravity waves in the ionosphere. Geophys Res Lett 49:e2021GL097170. https://doi.org/10.1029/2021GL097170
Dautermann T, Calais E, Lognonné P, Mattioli GS (2009a) Lithosphere– atmosphere–ionosphere coupling after the 2003 explosive eruption of the Soufriere Hills Volcano. Montserrat Geophys J Int 179:1537–1546. https://doi.org/10.1111/j.1365-246X.2009.04390.x
Dautermann T, Calais E, Mattioli GS (2009b) Global positioning system detection and energy estimation of the ionospheric wave caused by the 13 July 2003 explosion of the Soufriere Hills Volcano, Montserrat. J Geophys Res 114:B02202. https://doi.org/10.1029/2008JB005722
Duncombe J (2022) The surprising reach of Tonga's giant atmospheric waves. Eos. https://doi.org/10.1029/2022EO220050
Galvan DA, Komjathy A, Hickey MP, Stephens P, Snively J, Song YT, Butala MD, Mannucci AJ (2012) Ionospheric signatures of Tohoku-Oki tsunami of March 11, 2011: model comparisons near the epicenter. Radio Sci 47:RS4003. https://doi.org/10.1029/2012RS005023
Heki K (2006) Explosion energy of the 2004 eruption of the Asama Volcano, central Japan, inferred from ionospheric disturbances. Geophys Res Lett 33:L14303. https://doi.org/10.1029/2006GL026249
Hori T, Nishitani N, Miyoshi Y, Miyashita Y, Seki K, Segawa T, Hosokawa K, Yukimatu AS, Tanaka Y, Sato N, Kunitake M, Nagatsuma T (2013) An integrated analysis platform merging SuperDARN data within the THEMIS tool developed by ERG-Science Center (ERG-SC). Adv Polar Sci 24(1):69–77. https://doi.org/10.3724/SP.J.1085.2013.00069
Huba JD, Drob DP, Wu T-W, Makela JJ (2015) Modeling the ionospheric impact of tsunami-driven gravity waves with SAMI3: conjugate effects. Geophys Res Lett 42:5719–5726. https://doi.org/10.1002/2015GL064871
Imanishi Y (2022) Inertial effects due to eruption-induced atmospheric disturbances identified by superconducting gravimeter observations at Matsushiro, Japan. Earth Planet Space 74:54. https://doi.org/10.1186/s40623-022-01615-4
Inchin PA, Snively JB, Zettergren MD, Komjathy A, Verkhoglyadova OP, Ram S, Tulasi, (2020) Modeling of ionospheric responses to atmospheric acoustic and gravity waves driven by the 2015 Nepal Gorkha earthquake. J Geophys Res 25:e2019JA027200. https://doi.org/10.1029/2019JA027200
INGV RING Working Group (2016). RETE INTEGRATA NAZIONALE GNSS. https://doi.org/10.13127/RING.
IUGONET project team, Hayashi H, Koyama Y, Hori T, Tanaka Y, Abe S, Shinbori A, Kagitani M, Kouno T, Yoshida D, UeNo S, Kaneda N, Yoneda M, Umemura N, Tadokoro H, Motoba T (2013) Inter-university upper atmosphere global observation NETwork (IUGONET). Data Sci J 12:WDS179–WDS184. https://doi.org/10.2481/dsj.WDS-030
Iyemori T (1990) Storm-time magnetospheric currents inferred from mid-latitude geomagnetic field variations. J Geomag Geoelectr 42:1249–1265. https://doi.org/10.5636/jgg.42.1249
Iyemori T, Rao DRK (1996) Decay of the Dst field of geomagnetic disturbance after substorm onset and its implication to storm–substorm relation. Ann Geophys 14:608–618. https://doi.org/10.1007/s00585-996-0608-3
Jayachandran PT, Langley RB, MacDougall JW, Mushini SC, Pokhotelov D, Hamza AM, Mann IR, Milling DK, Kale ZC, Chadwick R, Kelly T, Danskin DW, Carrano CS (2009) The Canadian High Arctic Ionospheric Network (CHAIN). Radio Sci 44:RS0A03. https://doi.org/10.1029/2008RS004046
Jin S, Occhipinti G, Jin R (2015) GNSS ionospheric seismology: recent observation evidences and characteristics. Earth Sci Rev 147:54–64. https://doi.org/10.1016/j.earscirev.2015.05.003
Kakinami Y, Kamogawa M, Watanabe S, Odaka M, Mogi T, Liu J-Y, Sun Y, Yamada T (2013) Ionospheric ripples excited by superimposed wave fronts associated with Rayleigh waves in the thermosphere. J Geophys Res 118:905–911. https://doi.org/10.1002/jgra.50099
Kelley M (2009) The Earth's ionosphere: plasma physics and electrodynamics, 2nd edn. California Academic Press, San Diego
Koyama Y, Shinbori A, Tanaka Y, Hori T, Nosé M, Oimatsu S (2014) An interactive data language software package to calculate ionospheric conductivity by using numerical models. Comput Phys Commun 185:3398–3405. https://doi.org/10.1016/j.cpc.2014.08.011
Lin J-T, Rajesh PK, Lin CCH, Chou M-Y, Liu J-Y, Yue J, Hsiao T-Y, Tsai H-F, Chao H-M, Kung M-M (2022) Rapid conjugate appearance of the giant ionospheric Lamb wave signatures in the Northern Hemisphere after Hunga-Tonga volcano eruptions. Geophys Res Lett 49:e2022GL098222. https://doi.org/10.1029/2022GL098222
Liu JY, Chen CH, Lin CH, Tsai HF, Chen CH, Kamogawa M (2011) Ionospheric disturbances triggered by the 11 March 2011 M9.0 Tohoku earthquake. J Geophys Res 116:A06319. https://doi.org/10.1029/2011JA016761
Maeda K, Kato S (1966) Electrodynamics of the ionosphere. Space Sci Rev 5:57–79. https://doi.org/10.1007/bf00179215
Mayr HG, Harris I, Varosi F, Herrero FA (1984a) Global excitation of wave phenomena in a dissipative multiconstituent medium 1. Transfer function of the Earth's thermosphere. J Geophys Res 89:10929–10959. https://doi.org/10.1029/JA089iA12p10929
Mayr HG, Harris I, Varosi F, Herrero FA (1984b) Global excitation of wave phenomena in a dissipative multiconstituent medium 2. Impulsive perturbations in the Earth's thermosphere. J Geophys Res 89:10961–10986. https://doi.org/10.1029/JA089iA12p10961
Miyoshi Y, Hori T, Shoji M, Teramoto M, Chang TF, Segawa T, Umemura N, Matsuda S, Kurita S, Keika K, Miyashita Y, Seki K, Tanaka Y, Nishitani N, Kasahara S, Yokota S, Matsuoka A, Kasahara Y, Asamura K, Takashima T, Shinohara I (2018) The ERG science center. Earth Planet Space https://doi.org/10.1186/s40623-018-0867-8
Nakanishi K, Iyemori T, Taira K, Lühr H (2014) Global and frequent appearance of small spatial scale field-aligned currents possibly driven by the lower atmospheric phenomena as observed by the CHAMP satellite in middle and low latitudes. Earth Planet Space 66:40. https://doi.org/10.1186/1880-5981-66-40
Nakashima Y, Heki K, Takeo A, Cahyadi MN, Aditiya A, Yoshizawa K (2016) Atmospheric resonant oscillations by the 2014 eruption of the Kelud volcano, Indonesia, observed with the ionospheric total electron contents and seismic signals. Earth Planet Sci Lett 434:112–116. https://doi.org/10.1016/j.epsl.2015.11.029
NCEDC (2014) Northern California Earthquake Data Center. UC Berkeley Seismological Laboratory. Dataset. https://doi.org/10.7932/NCEDC
Nishioka M, Tsugawa T, Kubota M, Ishii M (2013) Concentric waves and short-period oscillations observed in the ionosphere after the 2013 Moore EF5

tornado. Geophys Res Lett 40:5581–5586. https://doi.org/10.1002/2013GL057963
Nishitani N, Ruohoniemi JM, Lester M, Baker JBH, Koustov AV, Shepherd SG, Chisham G, Hori T, Thomas EG, Makarevich RA, Marchaudon A, Ponomarenko P, Wild JA, Milan SE, Bristow WA, Devlin J, Miller E, Greenwald RA, Ogawa T, Kikuchi T (2019) Review of the accomplishments of mid-latitude Super Dual Auroral Radar Network (SuperDARN) HF radars. Prog Earth Planet Sci 6:27. https://doi.org/10.1186/s40645-019-0270-5
Noll C (2010) The crustal dynamics data information system: a resource to support scientific analysis using space geodesy. Adv Space Res 45:1421–1440. https://doi.org/10.1016/j.asr.2010.01.018
Otsuka Y, Kotake N, Tsugawa T, Shiokawa K, Ogawa T, Effendy S, Saito M, Kawamura T, Maruyama NH, Komolmis T (2006) GPS detection of total electron content variations over Indonesia and Thailand following the 26 December 2004 earthquake. Earth Planet Space 58:159–165. https://doi.org/10.1186/BF03353373
Otsuka Y, Onoma F, Shiokawa K, Ogawa T, Yamamoto M, Fukao S (2007) Simultaneous observations of nighttime medium-scale traveling ionospheric disturbances and E region field-aligned irregularities at midlatitude. J Geophys Res 112:A06317. https://doi.org/10.1029/2005JA011548
Otsuka Y, Suzuki K, Nakagawa S, Nishioka M, Shiokawa K, Tsugawa T (2013) GPS observations of medium-scale traveling ionospheric disturbances over Europe. Ann Geophys 31:163–172. https://doi.org/10.5194/angeo-31-163-2013
Pacific Northwest Geodetic Array (PANGA) (1996) GPS/GNSS Network and Geodesy Laboratory: Central Washington University, other/seismic network. Int Fed of Digit Seismogr Netw. https://doi.org/10.7914/SN/PW
Piñón DA, Gómez DD, Smalley R, Cimbaro SR, Lauría EA, Bevis MG (2018) The history, state, and future of the Argentine continuous satellite monitoring network and its contributions to geodesy in Latin America. Seismol Res Lett 89:475–482. https://doi.org/10.1785/0220170162
Poli P, Shapiro NM (2022) Rapid characterization of large volcanic eruptions: measuring the impulse of the Hunga Tonga Ha'apai explosion from teleseismic waves. Geophys Res Lett 49:e202GL098123. https://doi.org/10.1029/2022GL098123
RESIF (2017) RESIF-RENAG French National Geodetic Network. RESIF Reseau Sismologique Et Geodesique Francais. https://doi.org/10.15778/resif.rg
Richmond AD (1978) Gravity wave generation, propagation, and dissipation in the thermosphere. J Geophs Res 83:4131–4145. https://doi.org/10.1029/JA083iA09p04131
Richmond AD (1979) Ionospheric wind dynamo theory: a review. J Geomag Geoelectr 31:287–310. https://doi.org/10.5636/jgg.31.287
Rolland L, Lognonné P, Munekane H (2011) Detection and modeling of Rayleigh wave induced patterns in the ionosphere. J Geophys Res 116:A05320. https://doi.org/10.1029/2010JA016060
Saito S (2022) Ionospheric disturbances observed over Japan following the eruption of Hunga Tonga-Hunga Ha'apai on 15 January 2022. Earth Planet Space 74:57. https://doi.org/10.1186/s40623-022-01619-0
Saito A, Fukao S, Miyazaki S (1998a) High resolution mapping of TEC perturbations with the GSI GPS network over Japan. Geophys Res Lett 25:3079–3082. https://doi.org/10.1029/98GL52361
Saito A, Iyemori T, Blomberg LG, Yamamoto M, Takeda M (1998b) Conjugate observations of the mid-latitude electric field fluctuations with the MU radar and the Freja satellite. J Atmos Sol-Terr Phys 60:129–140. https://doi.org/10.1016/S1364-6826(97)00094-1
Saito A, Tsugawa T, Otsuka Y, Nishioka M, Iyemori T, Matsumura M, Saito S, Chen CH, Goi Y, Choosakul N (2011) Acoustic resonance and plasma depletion detected by GPS total electron content observation after the 2011 off the Pacific coast of Tohoku Earthquake. Earth Planet Space 63:863–867. https://doi.org/10.5047/eps.2011.06.034
Savastano G, Komjathy A, Verkhoglyadova O, Mazzoni A, Crespi M, Wei Y, Mannucci AJ (2017) Real-time detection of tsunami ionospheric disturbances with a stand-alone GNSS receiver: a preliminary feasibility demonstration. Sci Rep 7:46607. https://doi.org/10.1038/srep46607
Shinbori A, Nishimura Y, Tsuji Y, Kikuchi T, Araki T, Ikeda A, Uozumi T, Otadoy R, Utada H, Ishitsuka J, Trivedi N, Dutra S, Schuch N, Watari S, Nagatsuma T, Yumoto K (2010) Anomalous occurrence feature of the preliminary impulse of geomagnetic Sudden Commencement (SC) in the South Atlantic Anomaly (SAA) region. J Geophys Res 115:A08309. https://doi.org/10.1029/2009JA015035
Shinbori A, Otsuka Y, Sori T, Tsugawa T, Nishioka M (2020) Temporal and spatial variations of total electron content enhancements during a geomagnetic storm on 27 and 28 September 2017. J Geophys Res 125:e2019JA026873. https://doi.org/10.1029/2019JA026873
Shinbori A, Otsuka Y, Tsugawa T, Nishioka M, Kumamoto A, Tsuchiya F, Matsuda S, Kasahara Y, Matsuoka A (2021) Relationship between the locations of the midlatitude trough and plasmapause using GNSS-TEC and Arase satellite observation data. J Geophys Res 126:e2020JA028943. https://doi.org/10.1029/2020JA028943
Shiokawa K, Otsuka Y, Ihara C, Ogawa T, Rich FJ (2003) Ground and satellite observations of nighttime medium-scale traveling ionospheric disturbance at midlatitude. J Geophys Res 108:1145. https://doi.org/10.1029/2002JA009639
Shults K, Astafyeva E, Adourian S (2016) Ionospheric detection and localization of volcano eruptions on the example of the April 2015 Calbuco events. J Geophys Res 121:10303–10315. https://doi.org/10.1002/2016JA023382
Sori T, Shinbori A, Otsuka Y, Tsugawa T, Nishioka M (2019) Characteristics of GNSS total clectron content enhancements over the midlatitudes during a geomagnetic storm on 7 and 8 November 2004. J Geophys Res 124(10376–10):394. https://doi.org/10.1029/2019JA026713
Takenaka H, Sakashita T, Higuchi A, Nakajima T (2020) Development of geolocation correction for geostationary satellite observation by phase only correlation method using visible channel. Remote Sens 12:2472. https://doi.org/10.3390/rs12152472
Tanaka Y, Shinbori A, Hori T, Koyama Y, Abe S, Umemura N, Sato Y, Yagi M, Ueno S, Yatagai A, Ogawa Y, Miyoshi Y (2013) Analysis software for upper atmospheric data developed by the IUGONET project and its application to polar science. Adv Polar Sci 24:231–240. https://doi.org/10.3724/SPJ.1085.2013.00231
Tanioka Y, Yamanaka Y, Nakagaki T (2022) Characteristics of the deep sea tsunami excited offshore Japan due to the air wave from the 2022 Tonga eruption. Earth Planet Space 74:61. https://doi.org/10.1186/s40623-022-01614-5
Tapping KF (2013) The 10.7 cm solar radio flux (F10.7). Space Weather 11:394–406. https://doi.org/10.1002/swe.20064
Themens DR, Watson C, Žagar N, Vasylkevych S, Elvidge S, McCaffrey A, Prikryl P, Reid B, Wood A, Jayachandran PT (2022) Global propagation of ionospheric disturbances associated with the 2022 Tonga volcanic eruption. Geophys Res Lett 49:e202GL098158. https://doi.org/10.1029/2022GL098158
Tsugawa T, Saito A, Otsuka Y, Yamamoto M (2003) Damping of large-scale traveling ionospheric disturbances detected with GPS networks during the geomagnetic storm. J Geophys Res 108:1127. https://doi.org/10.1029/2002JA009433
Tsugawa T, Saito A, Otsuka Y, Nishioka M, Maruyama T, Kato H, Nagatsuma T, Murata KT (2011) Ionospheric disturbances detected by GPS total electron content observation after the 2011 off the Pacific coast of Tohoku Earthquake. Earth Planet Space https://doi.org/10.5047/eps.2011.06.035
World Data Center for Geomagnetism Kyoto, Nosé M, Iyemori T, Sugiura M, Kamei T (2015) Geomagnetic AE index. https://doi.org/10.17593/15031-54800
World Data Center for Geomagnetism Kyoto, Imajo S, Matsuoka A, Toh H, Iyemori T (2022) Mid-latitude geomagnetic indices ASY and SYM (ASY/SYM Indices). https://doi.org/10.14989/267216
Yamamoto Y, Ichii K, Higuchi A, Takenaka H (2020) Geolocation accuracy assessment of Himawari-8/AHI imagery for application to terrestrial monitoring. Remote Sens 12:1372. https://doi.org/10.3390/rs12091372
Yamazaki Y, Maute A (2017) Sq and EEJ—a review on the daily variation of the geomagnetic field caused by ionospheric dynamo currents. Space Sci Rev 206:299–405. https://doi.org/10.1007/s11214-016-0282-z

Publisher's Note